Research Square

Preprints are preliminary reports that have not undergone peer review.
They should not be considered conclusive, used to inform clinical practice,
or referenced by the media as validated information.

Improved Water/Polar Liquid Separation Performance of Graphene Oxide Membranes by Increasing the Starting Dispersion Concentration

Mikhail V. Matveev
Semenov Institute of Chemical Physics
Alexander V. Kaplin
Semenov Institute of Chemical Physics
Alexander A. Gulin
Semenov Institute of Chemical Physics
Tatiana S. Yankova
yankovats@my.msu.ru

Semenov Institute of Chemical Physics
Natalia A. Chumakova
Semenov Institute of Chemical Physics

Research Article

Keywords: graphene oxide membranes, water/polar liquid separation, membrane architecture, permeance and selectivity, lamellar ordering, layers ordering, spin probe technique

Posted Date: November 5th, 2026

DOI: https://doi.org/10.21203/rs.3.rs-11361707/v1

License: This work is licensed under a Creative Commons Attribution 4.0 International License.
Read Full License

Additional Declarations: No competing interests reported.

Improved Water/Polar Liquid Separation Performance of Graphene Oxide Membranes by Increasing the Starting Dispersion Concentration

Mikhail V. Matveev[1], Alexander V. Kaplin[1], Alexander A. Gulin[1], Tatiana S. Yankova[1*], and Natalia A. Chumakova[1]

[1] *N. N. Semenov Federal Research Center for Chemical Physics, Russian Academy of Sciences, Kosygin St. 4, Moscow, 119991, Russia*

Correspondence: yankovats@my.msu.ru

Abstract

Graphene oxide membranes (GOMs) are promising materials for separating water from polar organic liquids, but their separation performance depends strongly on membrane architecture and fabrication conditions. Three free-standing GOMs were prepared from the same starting graphene oxide dispersion at two concentrations: 2 mg mL^{-1} (isotropic) and 10 mg mL^{-1} (liquid-crystalline). The orientation of graphene oxide layers within the membranes was examined using spin-probe technique. For one membrane prepared from the concentrated dispersion, the nitroxide spin probe **H2** was added before filtration; for the other two membranes, the probe was introduced after membrane formation. Lamellar orientation was evaluated by SEM image analysis. The second-rank lamellar order parameters were similar for all three membranes (T_2 = 0.86–0.92), whereas the layer order parameters were lower (P_2 = 0.49–0.62) and differed between membranes prepared from isotropic and liquid-crystalline dispersions. Water-vapor permeance was comparable across all membranes, at approximately 0.046–0.052 mol m^{-2} s^{-1} bar^{-1}. In contrast, ethanol- and acetonitrile-vapor permeances decreased by a factor of approximately 4 and 2.5, respectively, for membranes prepared from the concentrated dispersion. Consequently, their water/ethanol selectivity increased from 12 for the isotropic-dispersion membrane to 36-43 for the membranes prepared from the concentrated dispersion, while water/acetonitrile selectivity increased from 9 to 21. These results show that increasing the starting dispersion concentration can substantially improve transport selectivity while maintaining similar water permeance. The two membranes prepared from the concentrated dispersion showed similar permeance and selectivity.

Keywords: graphene oxide membranes, water/polar liquid separation, membrane architecture, permeance and selectivity, lamellar ordering, layers ordering, spin probe technique.

1. Introduction

Graphene oxide membranes (GOMs) have been extensively studied [1-3] since Nair et al. reported exceptionally high permeability to water compared to other polar liquids and gases [4]. The high surface area of graphene oxide nanosheets, together with their numerous oxygen-containing functional groups, makes these materials promising for water desalination and dye removal [5-7], as well as for the separation of water and organic liquids [8-12].

Recently, GO-based membranes were shown to have high sorption and diffusion selectivity for water in water–ethanol mixtures [13]. Nevertheless, the transport properties of GOMs have varied substantially across studies over the past decade. Reported water permeabilities, for instance, vary by over four orders of magnitude [14]. This scatter may arise from differences in the composition of oxygen-containing functional groups, flake size distributions, and internal ordering of the membranes. Among these, the role of the orientational ordering of lamellae and graphene oxide layers remains the least studied, mainly because few methods are available for its quantitative determination.

Free-standing GOMs tens of micrometers thick have a hierarchical structure: they consist of lamellar stacks, each comprising several tens of individual graphene oxide layers. Consequently, a comprehensive study of the membrane structure requires quantitative characterization of the orientational ordering of both lamellae and individual layers. Recently, we developed two quantitative approaches for characterizing GOM architecture. The first is based on electron paramagnetic resonance (EPR) spectroscopy of stable nitroxide radicals (spin probes) adsorbed onto the oxidized graphene layers [15]. If the probe molecules adopt a well-defined orientation relative to the layer plane, their orientational order parameters reflect the ordering of the layers. Among the probes tested, nitroxides containing conjugated aromatic fragments with nitrogen atoms proved to be the most orientation-sensitive [16]. The second approach uses machine learning for quantitative analysis of scanning electron microscopy (SEM) images of membrane cross-sections, enabling determination of the lamellar orientation [17]. Together, these methods allow quantitative characterization of the membrane architecture at both the nanoscale (individual layers) and microscale (lamellar packets).

In a previous study, we showed that graphene oxide layer ordering and lamellar packing density independently and significantly influence GOM permeability and selectivity [18]. The starting GO dispersion concentration may affect both the packing density and the ordering of lamellae and GO layers. Increasing the concentration can lead to the formation of a liquid-crystalline phase in which the GO flakes are aligned relative to one another [19].

Only a few studies have demonstrated a substantial effect of the starting GO dispersion concentration on GOM performance in water nanofiltration [19-23]. However, the effect of the

starting dispersion concentration on the performance of free-standing membranes in water/polar-liquid separation has not been studied systematically.

The present study therefore investigates GOMs fabricated from a single graphene oxide dispersion at two different concentrations.

This work addresses the following questions:

(1) Do membranes prepared from dispersions at two concentrations (2 and 10 mg mL^{-1}) differ in their internal architecture and water/polar-liquid separation performance?

(2) Is water/polar-liquid separation performance reproducible for membranes prepared by the same method?

(3) Is the orientational distribution of the nitroxide spin probe in GOMs similar when the probe is introduced after membrane formation or during membrane preparation?

2. Materials and methods

2.1. Materials

The graphene oxide dispersion was prepared using an improved Hummers' method [24] and purified as described previously [25]. The C/O atomic ratio of graphene oxide determined by X-ray photoelectron spectroscopy (XPS) was 2.6.

The nitroxide spin probe (1,1,3,3-tetramethyl-2,3-dihydro-1H-pyrrolo[3,4-b]quinoxalin-2-yl)oxidanyl (**H2**) was synthesized as described in Ref. [26]. Our previous study showed that a conjugated aromatic fragment bearing two nitrogen atoms in the nitroxide molecule enhances its interaction with oxidized graphene layers and increases the orientational ordering of the probe molecules in the membrane [16].

HPLC-grade acetonitrile (purity > 99.99%) was supplied by RCI Labscan, and 96% ethanol was purchased from “Ruskhim”. Double-distilled water was used in all experiments.

2.2. Membrane fabrication and preparation of spin-probed samples

The GO dispersion was concentrated from 2 mg mL^{-1} to 10 mg mL^{-1} using hydrogel spheres, as described in [22]. Formation of a liquid-crystalline (LC) phase in the concentrated dispersion was detected by polarized optical microscopy (SDPTOP CX40M microscope) with crossed polarizers (Figure S1.1).

The membranes were prepared by vacuum-assisted self-assembly in a conventional glass filtration system consisting of a Büchner flask, a glass frit, and a porous Anodisk (Whatman) membrane used as the filtration substrate. Filtration with a water-jet pump typically took 7–12 h. After filtration, the resulting membrane was gently detached. The membrane thickness, measured

with an electronic micrometer at a relative humidity (RH) of 35%, was 25–35 μm, whereas the thickness estimated from SEM images was 15–20 μm (Figure 4). This difference is consistent with membrane swelling in humid air.

Three GOMs were studied. The first membrane (**ML**) was fabricated from a low-concentration isotropic dispersion (2 mg mL^{-1}), whereas the other two membranes (**MH1** and **MH2**) were prepared from the concentrated dispersion (10 mg mL^{-1}).

To prepare **ML** and **MH1** samples for EPR measurements, rectangular strips (4 × 10 mm) were cut from each membrane and immersed in a solution of **H2** in a 1:1 (volume) acetonitrile/water mixture at a concentration of ~$3.5 \cdot 10^{-3}$ mol/L. After 24 h in the solution, the membrane strips were removed and dried in air. The resulting samples contained approximately $3 \cdot 10^{16}$ radicals and yielded EPR spectra with a high signal-to-noise ratio.

To prepare the third membrane (**MH2)**, the **H2** spin probe was introduced into the concentrated dispersion prior to filtration. EPR spectra of the GO dispersion probed with **H2** nitroxide (see Fig. S3.1) show that **H2** molecules readily adsorb onto graphene oxide sheets. The resulting concentration of **H2** in the dispersion was found to be within the range of 0.01-0.05 mM.

The membrane preparation procedure is shown in Figure 1.

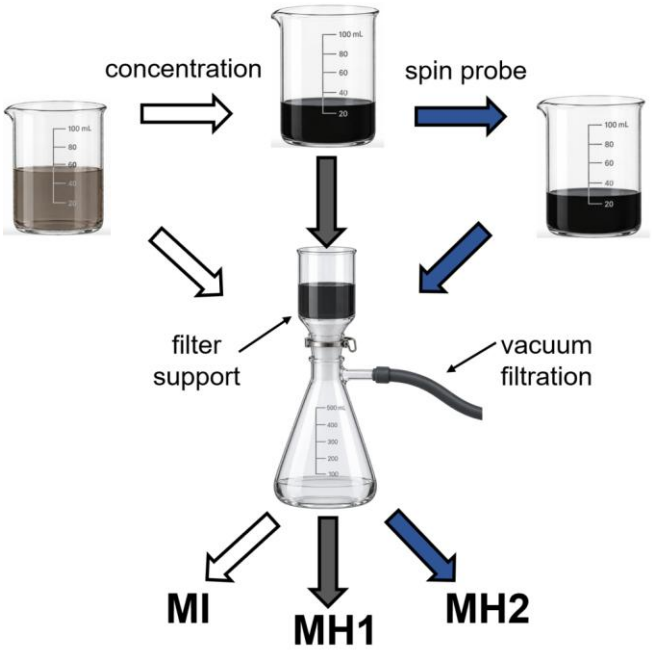


Figure 1. *Scheme of GOM preparation.*

2.3. SEM measurements and image analysis

The cross-sectional morphology of the membranes was examined using a Prisma E scanning electron microscope (SEM; Thermo Scientific, Czech Republic). Before imaging, the

samples were fixed on an L-shaped holder and coated with a 10 nm gold layer using a Q150R ES plus sputter coater (Quorum Technologies, Great Britain).

Quantitative analysis of SEM images of the GOM cross-sections was carried out using a machine-learning approach comprising two main stages. First, the images were segmented using a pre-trained UNet model [17], after which the resulting segmentation mask was binarized using a manually selected threshold to delineate the lamellar boundaries. Second, the angular distribution of the lamellae was calculated from the binarized mask, enabling determination of the orientational order parameters.

The orientational order parameters T_2 and T_4, characterizing lamellar ordering, were calculated by averaging the Chebyshev polynomials $T_j(\cos\beta)$ over the two-dimensional orientation distribution function $\rho_{2D}(\beta)$:

$$T_j = \int_0^{\pi} T_j(\cos\beta)\,\rho_{2D}(\beta)d\beta \qquad (1)$$

This procedure is described in detail in our earlier study [17]. The image processing software is freely available at [27, 28].

2.4. EPR spectroscopy and spectra simulation

EPR spectra were recorded using a Bruker EMXplus-10/12 PX X-band EPR spectrometer equipped with a nitrogen-flow temperature controller. The spin-probed membrane samples were fixed in a quartz holder, as described in [15]. The angular dependence of the EPR spectra was recorded at 105 K to suppress probe rotational motion, allowing the spectra to be simulated in the rigid limit. Using a Bruker automatic goniometer, the angle between the normal to the membrane surface and the spectrometer magnetic field was set in 10° steps with an accuracy of ±1°. The microwave power was set to 1 mW, and the magnetic-field modulation amplitude was 1 G. For each sample, at least 10 EPR spectra were recorded at different rotation angles.

The shape of EPR spectra in ordered media at low temperatures is governed by both the spin Hamiltonian parameters of the paramagnetic species and their orientational distribution. We used the spin Hamiltonian parameters of **H2** determined in our earlier work [16].

The angular dependences of the EPR spectra were simulated using the ODF3 program (freely available at [29]). Spectra acquired at different membrane orientations were fitted simultaneously, with the orientational order parameters of the probe molecules as adjustable parameters. To improve the accuracy of the order parameters, we used an iterative procedure in which the fits of the intense intrinsic GO signal and the weak nitroxide signals were refined sequentially. The simulation procedure is described in detail in [15].

In the fitting procedure, the orientational distribution function (ODF) of the nitroxide radicals was represented by a series of Legendre polynomials:

$$\rho(\beta) = \sum_{l=0}^{\infty} \frac{2l+1}{2} P_l P_l(cos\beta) \quad (2)$$

The order parameter of rank l is defined as the average value of the corresponding Legendre polynomial:

$$P_l = \int_0^{\pi} P_l(cos\beta)\, \rho(\beta) sin\beta d\beta \quad (3)$$

Here, β is the angle between the GOM surface normal and the magnetic z axis of the nitroxide molecule (see Figure 2a). For an axially symmetric distribution about the membrane surface normal, the distribution of the magnetic z axes is described by this single angle. Because of the symmetry of the nitroxide magnetic tensors, the EPR spectra are sensitive only to the even-order terms in Eq. 2.

At 105 K, the rotational mobility of the nitroxides is largely suppressed, so any variation in spectral line shape upon sample rotation reflects the orientational distribution of the probe molecules within the membrane. Figure 2a shows the nitroxide magnetic axes and the preferred orientation of the **H2** molecule with respect to the GOM surface. The angular dependence of the EPR spectra (Fig. 2b) shows that the magnetic z axes of the nitroxides are predominantly aligned with the membrane surface normal. The origin of the characteristic EPR spectral features of nitroxide spin probes is discussed in detail in [30].

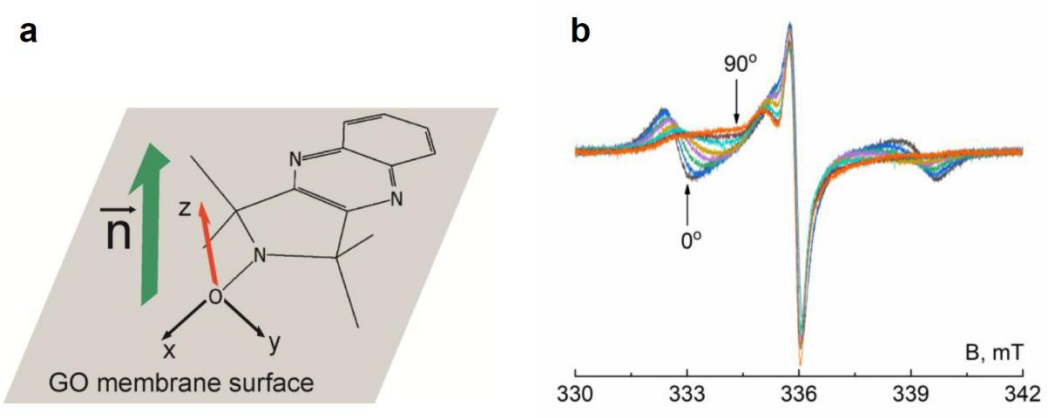


Figure 2. *(a) Orientation of the magnetic axes (x, y, z) of nitroxide* ***H2*** *relative to the GO membrane surface normal (green arrow); (b) EPR spectra of ML containing* ***H2****. The spectra were recorded at 105 K with the membrane surface normal rotated relative to the magnetic field.*

2.5. Measurements of GOM permeance to polar liquids

Membrane permeance was measured using a device (Fig. S2.1) in which the membrane was sealed above a vessel containing the liquid (V = 5 mL), with a saturated-vapor volume of

approximately 2 cm³ beneath the membrane. Transport through the membrane occurred from the vapor phase (gas pervaporation). The exposed membrane area was 78.5 mm².

The device was held in a TS-1/80 SPU thermostatic cabinet at 298 K (accuracy ±1 K). Temperature and humidity were monitored with a thermometer-hygrometer placed inside the thermostatic cabinet; relative humidity values were used to calculate the water vapor pressure inside the cabinet. The setup was weighed with a Mettler E240 analytical balance every 10–15 min to measure the mass loss over time. The corresponding mass-loss graphs are presented in Figure S2.2.

The driving force for transmembrane transport is the vapor-pressure difference between the two sides of the membrane. The slope obtained by linear regression of mass loss against time was normalized to the exposed membrane area (78.5 mm²) to determine the flux j through the membrane (Figure S2.2).

The permeance values (in mol m^{-2} bar^{-1} s^{-1}) were calculated as $P = {}^{j}/_{\Delta p}$, where Δp is the vapor-pressure difference above (p) and below (p^s) the membrane ($\Delta p = p^s - p$). The saturated vapor pressure below the membrane was calculated using the Antoine equation:

$$\lg p^s = A - \frac{B}{C + T}$$

The constants A, B, and C are given in Table S2.1 [31]. The values of p^s at room temperature (298 K) are 0.0313, 0.0776, and 0.1207 bar for water, ethanol, and acetonitrile, respectively.

The water-vapor pressure above the membrane was taken as the water-vapor pressure corresponding to the current relative humidity, according to the thermohygrometer readings (RH ~35%); thus, Δp_w = 0.0203 bar was used for water permeance measurements. The ethanol- and acetonitrile-vapor pressures above the membrane were assumed to be negligible because the thermostatic cabinet was ventilated.

Atmospheric moisture produces a reverse flux of water vapor (j_{rev}^w) through the membrane along with the outward flux (j_{dir}) of ethanol or acetonitrile. Thus, the observed flux is $j_{obs} = j_{dir} - j_{rev}^w$ in experiments with ethanol and acetonitrile. The values of j_{dir} for ethanol and acetonitrile (Table 1) were calculated as $j_{dir} = j_{obs} + j_{rev}^w$, where the reverse water flux was estimated from the measured water permeance as $j_{rev}^w = P_w \cdot \Delta p_w$; Δp_w for the acetonitrile experiment was taken as $RH \cdot p_w^s$ = 0.0110 bar. For the ethanol experiment, we accounted for the partial pressure of water over the azeotropic ethanol/water mixture. Using the water mole fraction χ = 0.10 in 96% ethanol and the water activity coefficient γ = 2.266 [32], we obtained a water partial pressure over the ethanol–water mixture of $p_w = \chi \cdot \gamma \cdot p_w^s$ = 0.0071 bar; thus, $\Delta p_w = 0.35 \cdot 0.0313 - 0.0071 = 0.0039$ bar for the ethanol experiment. The flux values are shown in Table 1. Ethanol permeance

for 96% solution was calculated as $j_{dir}/(p^s_{et} - p_w)$, acetonitrile permeance was calculated as j_{dir}/p^s_{acn}.

Table 1. Water, ethanol, and acetonitrile fluxes through the GOMs (values in 10^{-4} *mol* m^{-2} s^{-1}).

	j_w	$j^{ethanol}_{obs}$	$j^{ethanol}_{dir}$	$j^{acetonitrile}_{obs}$	$j^{acetonitrile}_{dir}$
ML	10.5	2.38	3.17	4.26	6.76
MH1	9.65	0.200	0.92	0.512	2.81
MH2	9.36	0.0489	0.75	0.322	2.54

3. Results and discussion

3.1. Structural characteristics of GOMs from SEM and the spin probe technique

SEM image analysis allows us to determine order parameters T_2, T_4, T_6… of GOM lamellae, which characterize structural ordering at the micrometer scale. At the same time, the orientation-sensitive spin probe technique provides the order parameters of individual oxidized graphene layers and thus characterizes membrane ordering at a smaller length scale. Due to the presence of sp^3-hybridized carbon atoms in the GO structure, graphene oxide layers tend to form waves or corrugations. The literature provides two estimates of the characteristic corrugation period of GO layers. Atomic force microscopy measurements of graphene oxide monolayers suggest a characteristic period of 10–20 nm [33], whereas molecular dynamics simulations for graphene oxide with C:O ratios of 2–3 yield values of approximately 5 nm [34]. These periods are 5–20 times the size of the **H2** probe (~1 nm). Given the flat and rigid structure of **H2**, the spin probes are expected to track the corrugations and provide order parameters P_2, P_4, … that are somewhat lower than those describing the overall layer alignment across the membrane. This structural model is shown schematically in Figure 3.

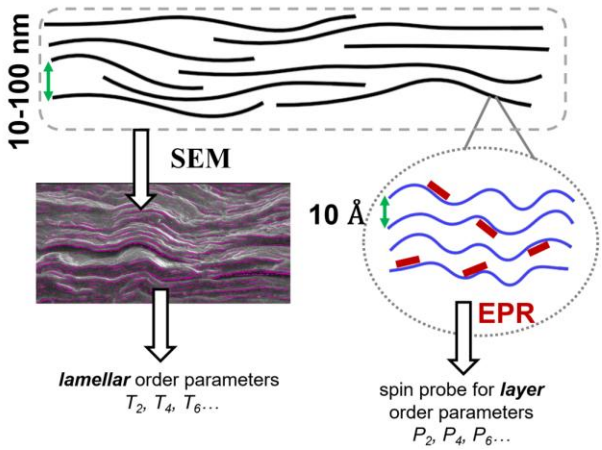


Figure 3. *Schematic representation of the hierarchical structure of GOMs.*

Representative SEM images of the three GOMs and the results of their analysis are presented in Figure 4. Up to 14 images for each sample were processed (See Table S4.1) to calculate the average order parameters. Lamellar order parameters were determined up to T_{10}. The T_2, T_4 and T_6 values were similar for the three GOMs, indicating comparable lamellar ordering.

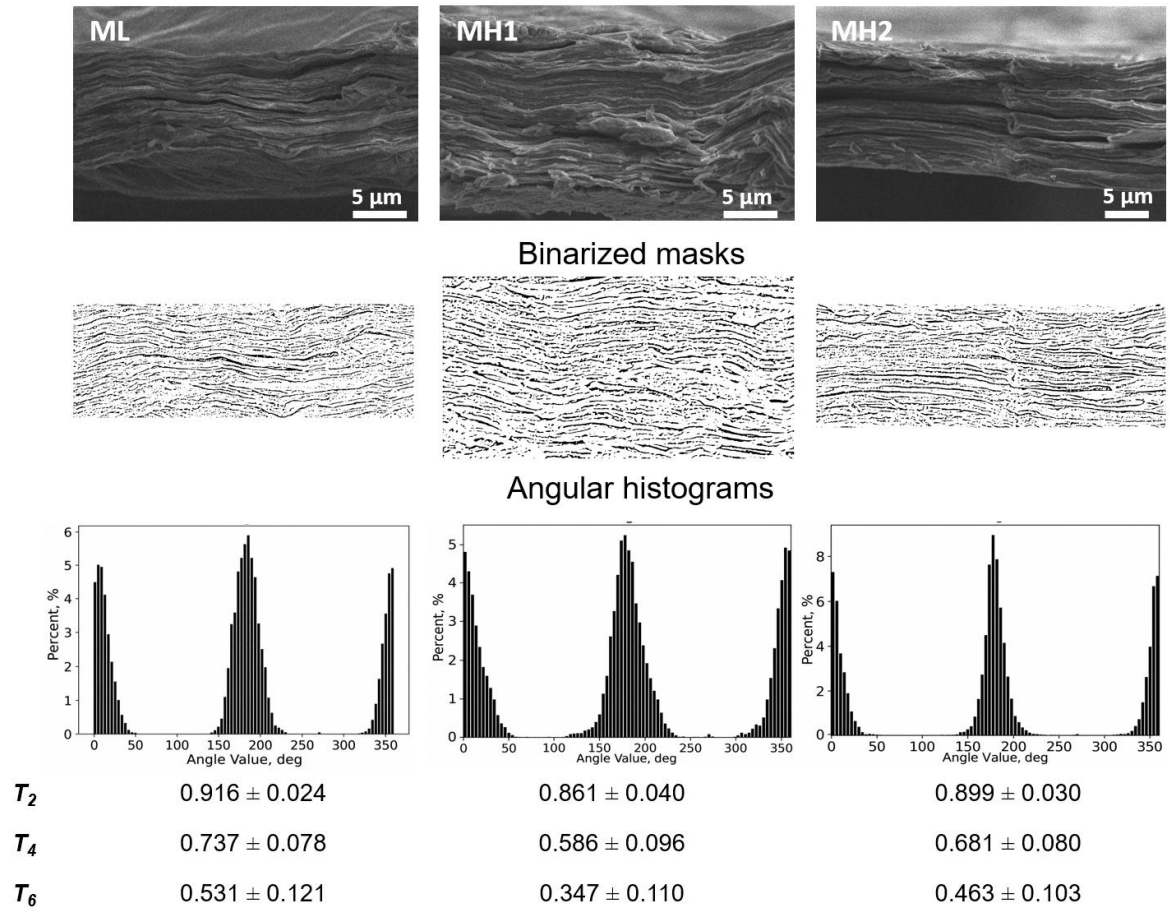
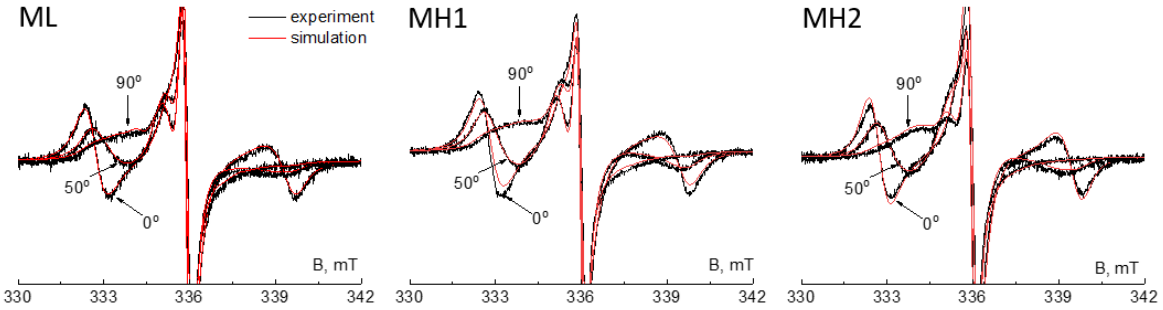


Figure 4. *SEM images of the GOMs and the corresponding segmentation masks and angular distributions.*

The angular dependences of the EPR spectra and the results of their simulation are presented in Figure 5. The simulation results of spectra deconvolution into nitroxide and GO components are shown in Figure S5.1. Joint simulation of the spectra yielded order parameters of ranks 2, 4, and 6 with sufficient reliability. Attempts to include higher-rank terms did not lead to a significant improvement in the fit, indicating that higher-rank features of the probe orientation distribution could not be resolved from these spectra.

The second-rank order parameters P_2 and T_2 characterize orientational ordering at different levels of GOM structure. The P_2 values obtained by EPR are lower than the T_2 values obtained by SEM. However, these parameters are defined using different polynomials and orientation distributions (Eqs. 1–3), so their numerical difference cannot be attributed directly to a difference

in structural ordering. We believe that layer corrugation contributes substantially to the distribution of local orientations sensed by EPR, while imperfect alignment of layers within lamellae may also contribute.



P_2	0.49	0.52	0.62
P_4	0.18	0.18	0.30
P_6	0.05	0.02	0.10

***Figure 5**. Angular dependences of the EPR spectra of the GOMs spin-probed with **H2** (black lines) and the results of their simulation (red lines). The spectra were recorded at 105 K at different angles between the membrane surface normal and the magnetic field. The values of uncertainties for the order parameters were estimated as ±10% for P_2, ±20% for P_4 and ±40% for P_6.*

The P_1 values (Figure 5) were slightly higher for both membranes prepared from the concentrated dispersion than for ML. The difference was small for **MH1** and more pronounced for **MH2**. This trend suggests that flake alignment in the liquid-crystalline dispersion can promote layer ordering in the membrane. The probe ordering in **MH2** was higher than in **MH1**. For **MH1**, the spin probes were introduced into the prepared membrane, whereas the **MH2** membrane was prepared from an aqueous dispersion already containing the spin probes. It is possible that not all interlayer spaces of the membrane are accessible to the probe molecules introduced from the solution.

3.2. Permeance and selectivity of the GOMs

The measured permeance values (Table 2 and Figure 6) show similar water-vapor permeance for the three GOMs, whereas ethanol- and acetonitrile-vapor permeances decrease significantly for GOMs prepared from the concentrated GO dispersion. The relative errors of the permeance values were estimated from linear regression analysis and were generally 1–6%, reaching 16% in the worst case. Table 2 also lists selectivity values for the water/ethanol and

water/acetonitrile pairs, calculated as ratios of the permeances of the individual substances. Since both substances (water and acetonitrile, or water and ethanol), which can mutually influence each other's permeability, were always present within the membrane during the experiment due to reverse water flow, the obtained values were supposed to be close to the real selectivities for separating mixtures of these substances. The main result of this study is a decrease in the permeance of ethanol and acetonitrile by a factor of approximately 4 and 2.5, respectively, for GOMs prepared from the concentrated dispersion. This leads to considerably higher water/ethanol and water/acetonitrile selectivity (Table 2). The two membranes prepared from the concentrated dispersion showed similar permeance and selectivity under the conditions studied.

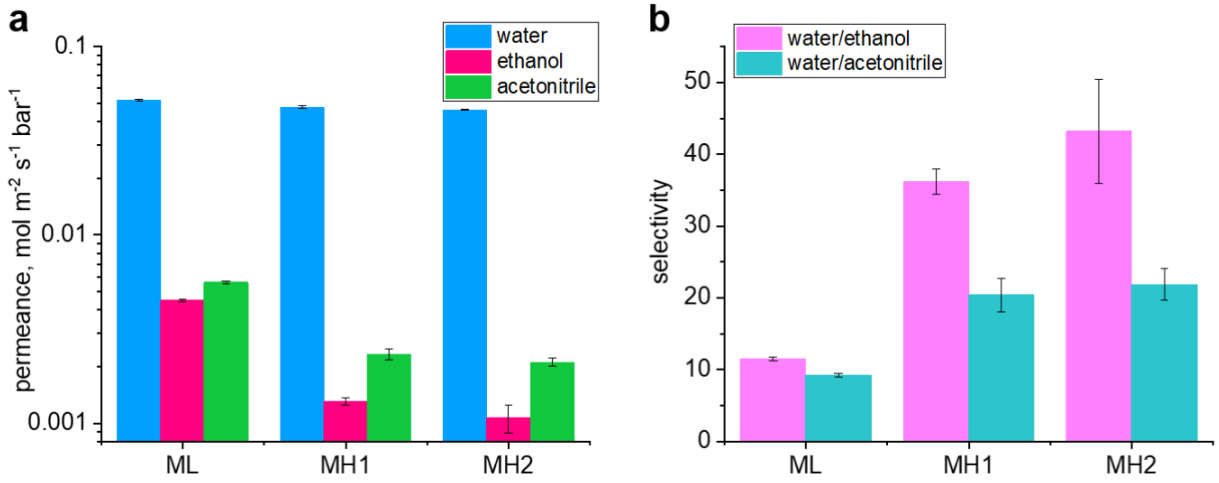


Figure 6. *(a) Permeance and (b) selectivity of the GOMs. Bars correspond to water (blue), ethanol (pink), and acetonitrile (green); selectivities are shown for water/ethanol (magenta) and water/acetonitrile (cyan).*

Membranes prepared from isotropic and liquid-crystalline dispersions differ only slightly in orientational ordering but exhibit substantially different transport properties. Differences in defect density may also contribute to their transport properties, but the present measurements cannot determine this characteristic.

Table 2. Functional properties of the GOMs

GOM	**Permeance, mol m^{-2} s^{-1} bar^{-1}**			**Selectivity**	
	water	**ethanol**	**acetonitrile**	**water/ethanol**	**water/acetonitrile**
ML	0.0518	0.00449	0.00560	11.5	9.2
MH1	0.0475	0.00131	0.00233	36.2	20.4
MH2	0.0461	0.00107	0.00211	43.2	21.8

4. Conclusions

Free-standing graphene oxide membranes were fabricated from the same starting dispersion at concentrations of 2 and 10 mg mL^{-1} and characterized at the levels of lamellae and individual GO layers. SEM analysis gave similar lamellar order parameters for the three membranes, whereas EPR measurements revealed slightly higher layer order parameters for the membranes prepared from the concentrated dispersion. The most pronounced effect of increasing the starting dispersion concentration was on the transport of organic vapors. While water permeance remained nearly unchanged, ethanol and acetonitrile permeances decreased substantially for the membranes prepared from the concentrated dispersion. This resulted in higher water/ethanol and water/acetonitrile selectivity. The two membranes prepared from the concentrated dispersion showed similar permeance and selectivity under the conditions studied.

The results indicate that controlling the concentration of the starting GO dispersion is a potentially effective way to improve water/polar-liquid separation selectivity without a substantial loss in water permeance.

Acknowledgements

The authors acknowledge support from the Lomonosov Moscow State University development program for access to the Bruker EMXplus-10/12 PX X-band EPR spectrometer.

Funding

This work was supported by the Russian Science Foundation (project No. 26-13-00023).

Competing Interests

The authors have no relevant financial or non-financial interests to disclose.

Author Contributions

All authors contributed to the study conception and design. M.V.M. conducted the core experiments and performed the simulations. Data collection, processing and analysis were performed by M.V.M., T.S.Y. and N.A.C; A.V.K. and A.A.G. conducted necessary experiments. The first draft of the manuscript was written by T.S.Y.; M.V.M. and N.A.C. edited the manuscript. All authors read and approved the final manuscript.

Data Availability

The datasets generated during and/or analyzed during the current study are available from the corresponding author on reasonable request.

References

(1) Liu, G.; Jin, W.; Xu, N. Graphene-Based Membranes. *Chem. Soc. Rev.* **2015**, *44* (15), 5016–5030. https://doi.org/10.1039/C4CS00423J

(2) Kang, Y.; Xia, Y.; Wang, H.; Zhang, X. 2D Laminar Membranes for Selective Water and Ion Transport. *Adv. Funct. Mater.* **2019**, *29* (29), 1902014. https://doi.org/10.1002/adfm.201902014

(3) An, Y.-C.; Gao, X.-X.; Jiang, W.-L.; Han, J.-L.; Ye, Y.; Chen, T.-M.; Ren, R.-Y.; Zhang, J.-H.; Liang, B.; Li, Z.-L.; Wang, A.-J.; Ren, N.-Q. A Critical Review on Graphene Oxide Membrane for Industrial Wastewater Treatment. *Environ. Res.* **2023**, *223*, 115409. https://doi.org/10.1016/j.envres.2023.115409

(4) Nair, R. R.; Wu, H. A.; Jayaram, P. N.; Grigorieva, I. V.; Geim, A. K. Unimpeded Permeation of Water Through Helium-Leak–Tight Graphene-Based Membranes. *Science* **2012**, *335* (6067), 442–444. https://doi.org/10.1126/science.1211694

(5) Yousefi, N.; Lu, X.; Elimelech, M.; Tufenkji, N. Environmental Performance of Graphene-Based 3D Macrostructures. *Nat. Nanotechnol.* **2019**, *14* (2), 107–119. https://doi.org/10.1038/s41565-018-0325-6

(6) Tiwary, S. K.; Singh, M.; Chavan, S. V.; Karim, A. Graphene Oxide-Based Membranes for Water Desalination and Purification. *Npj 2D Mater. Appl.* **2024**, *8* (1), 27. https://doi.org/10.1038/s41699-024-00462-z

(7) Joshi, R. K.; Carbone, P.; Wang, F. C.; Kravets, V. G.; Su, Y.; Grigorieva, I. V.; Wu, H. A.; Geim, A. K.; Nair, R. R. Precise and Ultrafast Molecular Sieving through Graphene Oxide Membranes. *Science* **2014**, *343* (6172), 752–754. https://doi.org/10.1126/science.1245711

(8) Liang, B.; He, X.; Hou, J.; Li, L.; Tang, Z. Membrane Separation in Organic Liquid: Technologies, Achievements, and Opportunities. *Adv. Mater.* **2019**, *31* (45), 1806090. https://doi.org/10.1002/adma.201806090

(9) Yang, Q.; Su, Y.; Chi, C.; Cherian, C. T.; Huang, K.; Kravets, V. G.; Wang, F. C.; Zhang, J. C.; Pratt, A.; Grigorenko, A. N.; Guinea, F.; Geim, A. K.; Nair, R. R. Ultrathin Graphene-Based Membrane with Precise Molecular Sieving and Ultrafast Solvent Permeation. *Nat. Mater.* **2017**, *16* (12), 1198–1202. https://doi.org/10.1038/nmat5025

(10) Huang, K.; Liu, G.; Lou, Y.; Dong, Z.; Shen, J.; Jin, W. A Graphene Oxide Membrane with Highly Selective Molecular Separation of Aqueous Organic Solution. *Angew. Chem.* **2014**, *126* (27), 7049–7052. https://doi.org/10.1002/ange.201401061

(11) Nie, L.; Chuah, C. Y.; Bae, T.; Lee, J. Graphene-Based Advanced Membrane Applications in Organic Solvent Nanofiltration. *Adv. Funct. Mater.* **2021**, *31* (6), 2006949. https://doi.org/10.1002/adfm.202006949

(12) Huang, K.; Liu, G.; Shen, J.; Chu, Z.; Zhou, H.; Gu, X.; Jin, W.; Xu, N. High-Efficiency Water-Transport Channels Using the Synergistic Effect of a Hydrophilic Polymer and Graphene Oxide Laminates. *Adv. Funct. Mater.* **2015**, *25* (36), 5809–5815. https://doi.org/10.1002/adfm.201502205

(13) Gurianov, K. E.; Astvatsaturov, D. A.; Lesnykh, A. A.; Chumakov, A.; Eliseev, A. A.; Kolesnik, I. V.; Zhang, L.; Chumakova, N. A.; Eliseev, A. A. Sorption and Diffusion Selectivity of Water-Ethanol Transport in Graphene Oxide Membranes. *J. Membr. Sci.* **2026**, *741*, 125016. https://doi.org/10.1016/j.memsci.2025.125016

(14) Amadei, C. A.; Vecitis, C. D. How to Increase the Signal-to-Noise Ratio of Graphene Oxide Membrane Research. *J. Phys. Chem. Lett.* **2016**, *7* (19), 3791–3797. https://doi.org/10.1021/acs.jpclett.6b01829

(15) Chumakova, N. A.; Vorobiev, A. Kh.; Astvatsaturov, D. A.; Yankova, T. S.; Rebrikova, A. T.; Matveev, M. V. Quantitative Determination of the Orientational Ordering of Graphene Oxide Membranes by the Spin Probe Technique. *Phys. Chem. Chem. Phys.* **2022**, *24* (8), 4881–4890. https://doi.org/10.1039/d1cp05417a

(16) Chumakova, N. A.; Kalai, T.; Rebrikova, A. T.; Sár, C.; Kokorin, A. I. Novel Orientation-Sensitive Spin Probes for Graphene Oxide Membranes Study. *Membranes* **2022**, *12* (12). https://doi.org/10.3390/membranes12121241

(17) Marnautov, N. A.; Matveev, M. V.; Gulin, A. A.; Kálai, T.; Bognár, B.; Rebrikova, A. T.; Chumakova, N. A. Orientational Ordering of Graphene Oxide Membranes by a Spin Probe Technique and SEM

Image Analysis. *J. Phys. Chem. C* **2024**, *128* (6), 2543–2550. https://doi.org/10.1021/acs.jpcc.3c07127
(18) Yankova, T. S.; Chichulin, S. N.; Kaplin, A. V.; Matveev, M. V.; Dvoryak, S. V.; Kuzovchikov, S. M.; Gatin, A. K.; Kálai, T.; Chumakova, N. A. Architecture of Graphene Oxide Membranes and Its Influence on the Selective Permeance to Water, Ethanol, and Acetonitrile. *Chem. Phys. Lett.* **2025**, *880*, 142397. https://doi.org/10.1016/j.cplett.2025.142397
(19) Lin, A. C.; Xie, F.; McCarthy, L. J.; Rodgers, D. R.; Hoff, K. G.; Von Welczeck, M. R.; Zhai, S.; Saw, A. C.; Scott, G. E.; Zhang, S. Photonic Liquid Crystals of Graphene Oxide for Fast Membrane Nanofiltration. *Carbon Trends* **2022**, *7*, 100150. https://doi.org/10.1016/j.cartre.2022.100150
(20) Pla, R.; Fernández-Márquez, M.; Baeza, J. A.; Calvo, L.; Alonso-Morales, N.; Gilarranz, M. A. Understanding the Role of Graphene Oxide Dispersion on Tuning Membrane Properties for Water Nanofiltration. *Environ. Technol. Innov.* **2025**, *37*, 104017. https://doi.org/10.1016/j.eti.2025.104017
(21) Pla, R.; Alonso-Morales, N.; Baeza, J. A.; Calvo, L.; Gilarranz, M. A. Removal of PFAS from Complex Matrix Water by Filtration with Supported Graphene Oxide Membranes. *J. Environ. Chem. Eng.* **2025**, *13* (6), 120225. https://doi.org/10.1016/j.jece.2025.120225
(22) Akbari, A.; Sheath, P.; Martin, S. T.; Shinde, D. B.; Shaibani, M.; Banerjee, P. C.; Tkacz, R.; Bhattacharyya, D.; Majumder, M. Large-Area Graphene-Based Nanofiltration Membranes by Shear Alignment of Discotic Nematic Liquid Crystals of Graphene Oxide. *Nat. Commun.* **2016**, *7*. https://doi.org/10.1038/ncomms10891
(23) Pedico, A.; Fontana, M.; Bianco, S.; Kara, S.; Periolatto, M.; Carminati, S.; Pirri, C. F.; Tresso, E.; Lamberti, A. Graphene Oxide Membranes for Trace Hydrocarbon Contaminant Removal from Aqueous Solution. *Nanomaterials* **2020**, *10* (11), 2242. https://doi.org/10.3390/nano10112242
(24) Marcano, D. C.; Kosynkin, D. V.; Berlin, J. M.; Sinitskii, A.; Sun, Z.; Slesarev, A.; Alemany, L. B.; Lu, W.; Tour, J. M. Improved Synthesis of Graphene Oxide. *ACS Nano* **2010**, *4* (8), 4806–4814. https://doi.org/10.1021/nn1006368
(25) Ratova, D. M. V.; Mikheev, I. V.; Chermashentsev, G. R.; Maslakov, K. I.; Kottsov, S. Y.; Stolbov, D. N.; Maksimov, S. V.; Sozarukova, M. M.; Proskurnina, E. V.; Proskurnin, M. A. Green and Sustainable Ultrasound-Assisted Anodic Electrochemical Preparation of Graphene Oxide Dispersions and Their Antioxidant Properties. *Mol. Basel Switz.* **2023**, *28* (7). https://doi.org/10.3390/molecules28073238
(26) Isbera, M.; Bognár, B.; Gulyás-Fekete, G.; Kish, K.; Kálai, T. Syntheses of Pyrazine-, Quinoxaline-, and Imidazole-Fused Pyrroline Nitroxides. *Synthesis* **2019**, *51* (23), 4463–4472. https://doi.org/10.1055/s-0039-1690678
(27) Marnautov, N. A. NMar33. https://github.com/NMar33/layerseg
(28) Marnautov, N. A. OrientLayer Analyser. https://colab.research.google.com/drive/1yl9UGMGGjR3cFTzAqibZsER3trWyC4h_?usp=sharing
(29) Vorobiev, A. K. ODF3. http://www.chem.msu.ru/rus/lab/chemkin/ODF3
(30) Bordignon, E. EPR Spectroscopy of Nitroxide Spin Probes. In *eMagRes*; Harris, R. K., Wasylishen, R. L., Eds.; John Wiley & Sons, Ltd: Chichester, UK, 2017; pp 235–254. https://doi.org/10.1002/9780470034590.emrstm1513
(31) Dortmund Data Bank. *http://ddbonline.ddbst.com/AntoineCalculation/AntoineCalculationCGI.exe*.
(32) D'Avila, S. G.; Silva, R. S. F. Isothermal Vapor-Liquid Equilibrium Data by Total Pressure Method. Systems Acetaldehyde-Ethanol, Acetaldehyde-Water, and Ethanol-Water. *J. Chem. Eng. Data* **1970**, *15* (3), 421–424. https://doi.org/10.1021/je60046a010
(33) Paredes, J. I.; Villar-Rodil, S.; Solís-Fernández, P.; Martínez-Alonso, A.; Tascón, J. M. D. Atomic Force and Scanning Tunneling Microscopy Imaging of Graphene Nanosheets Derived from Graphite Oxide. *Langmuir* **2009**, *25* (10), 5957–5968. https://doi.org/10.1021/la804216z
(34) Bu, Y.; Li, K.; Xiong, Z.; Liang, Z.; Zhang, J.; Bi, Z.; Zhang, H. Evolution of Layer Distance and Structural Arrangement of Graphene Oxide with Various Oxygen Content and Functional Types in Low Temperature: A ReaxFF Molecular Dynamics Simulation. *Appl. Surf. Sci.* **2022**, *572*, 151390. https://doi.org/10.1016/j.apsusc.2021.151390

Supplementary Files

This is a list of supplementary files associated with this preprint. Click to download.

- matveevSI.docx